Electric Sail Trajectory Design with Bezier Curve-based Shaping Approach

Mingying Huo[1], Giovanni Mengali[2], Alessandro A. Quarta[2]*, Naiming Qi[1]

[1] *Department of Aerospace Engineering – Harbin Institute of Technology, 92 Xidazhi Street, Harbin 150001, China*

[2] *Department of Civil and Industrial Engineering, University of Pisa, I-56122 Pisa, Italy*

Abstract

The aim of this paper is to propose a shape-based method in which the concept of Bezier curve is used to efficiently design the three-dimensional interplanetary trajectory of a spacecraft whose primary propulsion system is an Electric Solar Wind Sail. The latter is a propellantless propulsion concept that consists of a spinning grid of tethers, kept at a high positive potential by a power source and maintained stretched by the centrifugal force. The proposed approach approximates the time variation of the components of the spacecraft position vector using a Bezier curve function, whose geometric coefficients are calculated by optimizing the total flight time with standard numerical methods and enforcing the boundary conditions of a typical interplanetary rendezvous mission. The paper also discusses a geometrical approach to include, in the optimization process, the propulsive acceleration vector constraints obtained with the latest Electric Solar Wind Sail thrust model.

Keywords: Electric Solar Wind Sail, Trajectory approximation, Preliminary mission analysis, Bezier Curve-based Shaping Approach

Nomenclature

$\boldsymbol{a}$	=	propulsive acceleration, with $a = \|\boldsymbol{a}\|$ [mm/s²]
a_c	=	characteristic acceleration [mm/s²]
$\tilde{a}_r, \tilde{a}_t$	=	dimensionless radial and transverse acceleration components
$B_{i,j}$	=	basis functions of the Bezier curve, see Eqs. (42)
$\boldsymbol{f}$	=	dimensionless vector function describing the spacecraft dynamics
J	=	performance index
m	=	Legendre-Gauss discretization points
N	=	total number of unknowns
N_P	=	number of unknown geometric coefficients
$\hat{\boldsymbol{n}}$	=	normal unit vector
n	=	order of the Bezier curve
O	=	Sun's center-of-mass
$P_{i,j}$	=	geometric coefficient of the Bezier curve
$\boldsymbol{r}$	=	spacecraft position vector [au]
r	=	Sun-spacecraft distance [au]
$r_\oplus$	=	reference distance [au]
$\mathcal{S}$	=	admissible region; see Fig. 7
t	=	time [days]

*Corresponding author

Email addresses: huomingying123@gmail.com (Mingying Huo[1]), g.mengali@ing.unipi.it (Giovanni Mengali[2]), a.quarta@ing.unipi.it (Alessandro A. Quarta[2]), qinaimingok_hit@163.com (Naiming Qi[1])

$\mathcal{T}_C(O; \rho, \theta, z)$	$=$	cylindrical reference frame
$\mathcal{T}_I(O; x_I, y_I, z_I)$	$=$	inertial reference frame
$\mathcal{T}_O(S; x_O, y_O, z_O)$	$=$	orbital reference frame
$\boldsymbol{u}$	$=$	control vector
$\boldsymbol{v}$	$=$	spacecraft velocity vector $[\text{km/s}]$
$\boldsymbol{x}$	$=$	dimensionless state vector
z	$=$	axial coordinate $[\text{au}]$
α_n	$=$	sail pitch angle $[\text{rad}]$
κ	$=$	thrust modulation parameter
$\mu_\odot$	$=$	Sun's gravitational parameter $[\text{km}^3/\text{s}^2]$
ρ	$=$	radial distance $[\text{au}]$
ϕ	$=$	azimuth angle $[\text{rad}]$
θ	$=$	polar angle $[\text{rad}]$
σ	$=$	sail clock angle $[\text{rad}]$
τ	$=$	dimensionless time

Subscripts

0	$=$	initial, parking orbit
app	$=$	approximated
f	$=$	final, target orbit
ρ, θ, z	$=$	components in $\mathcal{T}_C$
x_O, y_O, z_O	$=$	components in $\mathcal{T}_O$

Superscripts

$\cdot$	$=$	time derivative
$'$	$=$	derivative with respect to τ
$\wedge$	$=$	unit vector
$\smile$	$=$	dimensionless

1. Introduction

A rapid initial trajectory design is a fundamental requirement for preliminary mission analysis and optimization of a spacecraft with a low-thrust propulsion system [1, 2, 3]. In fact, irrespective of whether an indirect or a direct approach is used to obtain an optimal trajectory, a reasonable initial guess for the state and co-state variables is required to ensure the convergence of the numerical method toward an optimal value of a given performance index [4]. Also, since both indirect and direct methods are usually demanding in terms of computational time, they are not well suited for rapid feasibility assessment [5, 6] in the preliminary phase of mission design, when a great number of flight scenarios need to be analyzed and compared.

For this reason, new techniques for rapid trajectory generation have emerged in recent years, mostly pushed forward by shape-based methods [7], in which the trajectory shape is in advance chosen as a given analytic function. In that way, the spacecraft equations of motion and the boundary constraints are simultaneously satisfied by computing a finite set of unknown parameters that define the shape of the analytic function used for approximating the generic state variable [8]. The shape-based approach to trajectory design was first proposed by Petropoulos and Longuski [7], who selected an exponential sinusoid function to describe the trajectory of a spacecraft propelled by a solar electric (power limited) thruster. Fifth- and sixth-order inverse polynomials were then proposed by Wall and Conway [8] to match the spacecraft position and velocity at its trajectory boundaries, whereas Xie et al. [9] suggested a rapid shaping method based on the radial coordinate form of the initial and target orbits. More recently, Taheri and Abdelkhalik [10] developed a flexible approach that exploits a finite Fourier series approximation to shape the spacecraft trajectory in a three-dimensional mission scenario, taking into account the thrust vector constraints. In

the finite Fourier series method [11], the time variation of the spacecraft states are expanded by means of Fourier series, of which the coefficients are obtained by optimizing a given performance index, such as the total propellant consumption or the flight time, and by enforcing the assigned boundary constraints.

The aim of this paper is to propose a rapid shape-based method where the concept of Bezier curve [12, 13] is used to efficiently design the three-dimensional interplanetary trajectory of a spacecraft propelled by an Electric Solar Wind Sail (E-sail). The latter is a propellantless and continuous-thrust propulsion concept [14, 15, 16], which essentially consists of a spinning grid of tethers, kept at a high positive potential by a power source and maintained stretched by the centrifugal force effect; see Fig. 1. In the proposed approach,
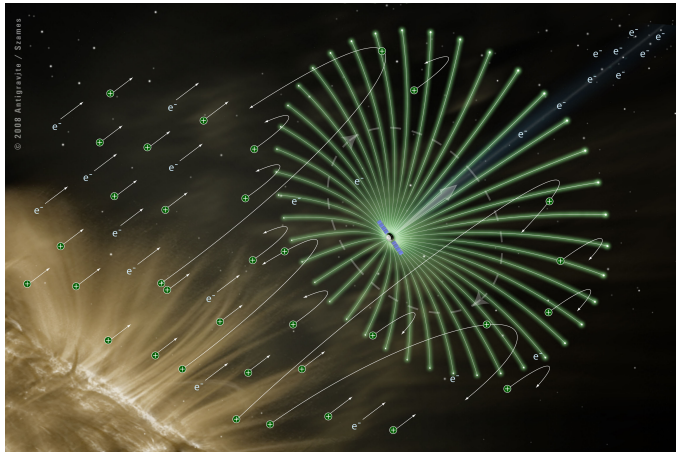

Figure 1: Electric Solar Wind Sail concept (artist's impression). Courtesy of Alexandre Szames, Antigravite (Paris).

the time variation of the components of the spacecraft position vector are assumed to have the form of Bezier curve functions. For a typical interplanetary rendezvous mission scenario, twelve Bezier coefficients may be analytically calculated by enforcing the boundary constraints on the spacecraft position and velocity vector. The other (unknown) coefficients are instead obtained by minimizing the total flight time and by taking into account the constraints on the E-sail thrust vector magnitude and direction [17, 18, 19, 20]. In particular, it is shown how those constraints may be fitted into the trajectory optimization algorithm by means of a compact, geometrical approach. The results obtained with the Bezier-based approximation method are then used as a first guess for a numerical refinement through a trajectory optimization software based on the Gauss pseudospectral method (GPM).

The remainder of the paper is organized as follows. Section 2 introduces the orbital dynamics of the E-sail in a cylindrical coordinate system. In section 3, the Bezier-based approximation method is applied to the initial guess of the three-dimensional optimal trajectory of the E-sail by introducing the thrust vector constraint. In section 4, the proposed approach is tested in an Earth-Mars interplanetary transfer and in a rendezvous mission with 3671 Dionysus asteroid of a spacecraft equipped with a medium performance E-sail. Finally, the last section contains some concluding remarks.

2. E-sail-based spacecraft orbital dynamics

Consider a spacecraft S whose primary propulsion system is an E-sail, and introduce a heliocentric-ecliptic (inertial) reference frame $\mathcal{T}_I(O; x_I, y_I, z_I)$, in which the origin coincides with the Sun's center of mass O, the x_I-axis points the vernal equinox, and the z_I-axis points towards the north ecliptic pole; see Fig. 2.

The propulsive acceleration vector $\boldsymbol{a}$ can be written in a compact, analytical, form as [19]

$$\boldsymbol{a} = \frac{\kappa \, a_c}{2} \left(\frac{r_\oplus}{r} \right) [\hat{\boldsymbol{r}} + (\hat{\boldsymbol{r}} \cdot \hat{\boldsymbol{n}}) \, \hat{\boldsymbol{n}}] \tag{1}$$

where $\kappa \in [0, 1]$ is the dimensionless thrust modulation parameter (with $\kappa = 0$ when the onboard electron gun is switched off), $\hat{\boldsymbol{r}} \triangleq \boldsymbol{r}/r$ is the spacecraft position unit vector, where r is the Sun-spacecraft distance

3
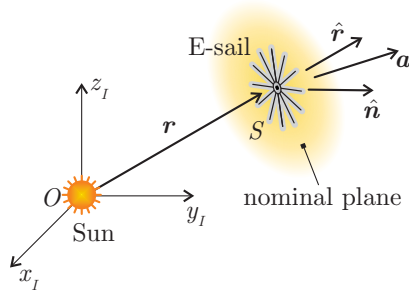
Figure 2: Inertial reference frame $\mathcal{T}_I$ and E-sail conceptual scheme. Adapted from Ref. [21].

(with $r_\oplus \triangleq 1\,\text{au}$), and $\hat{\boldsymbol{n}}$ is the unit vector normal to the sail nominal plane in the direction opposite to the Sun; see Fig. 2. In Eq. (1), a_c is the spacecraft characteristic acceleration, defined as the maximum value of the propulsive acceleration magnitude $a \triangleq \|\boldsymbol{a}\|$ at a distance $r = r_\oplus$. The value of a_c is a typical performance parameter [22], which depends on the E-sail design characteristics (such as the number of tethers, and the grid electric voltage), and the spacecraft mass budget [23]. Note that κ models the E-sail intrinsic capability of modulating, within some limits and with a finite number of admissible levels [24], the thrust magnitude by changing the grid electric voltage. For this reason, a value of κ that continuously ranges between 0 (no thrust) and 1 (full thrust) may be thought of as a useful mathematical approximation of the actual E-sail behaviour discussed in Refs. [25, 26].

The E-sail attitude is conveniently described by introducing an orbital reference frame $\mathcal{T}_O(S; x_O, y_O, z_O)$, whose origin coincides with the spacecraft center of mass, the z_O-axis is along the Sun-spacecraft line (which coincides with the approximate direction of propagation of the solar wind), while the y_O-axis is perpendicular to the (z_O, z_I) plane and has the same direction as the spacecraft inertial velocity; see Fig. 3. The components
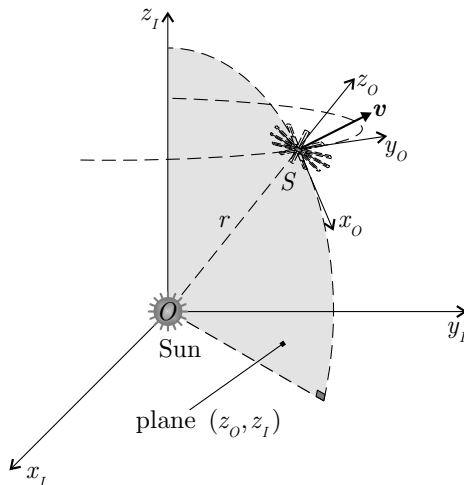

Figure 3: Orbital reference frame $\mathcal{T}_O$.

of $\boldsymbol{r}$ and $\hat{\boldsymbol{n}}$ in $\mathcal{T}_O$ are

$$[\boldsymbol{r}]_{\mathcal{T}_O} = \begin{bmatrix} 0 \\ 0 \\ r \end{bmatrix} \qquad , \qquad [\hat{\boldsymbol{n}}]_{\mathcal{T}_O} = \begin{bmatrix} \sin\alpha_n \, \cos\sigma \\ \sin\alpha_n \, \sin\sigma \\ \cos\alpha_n \end{bmatrix} \tag{2}$$

where $\alpha_n \in [0, \pi/2]\,\text{rad}$ is the sail pitch angle, that is, the angle between $\hat{\boldsymbol{n}}$ and the Sun-spacecraft line, and $\sigma \in [0, 2\pi]\,\text{rad}$ is the sail clock angle, that is, the angle (measured counterclockwise from the x_O-axis) between the x_O-axis and the projection of $\hat{\boldsymbol{n}}$ on the (x_O, y_O) plane; see Fig. 4.
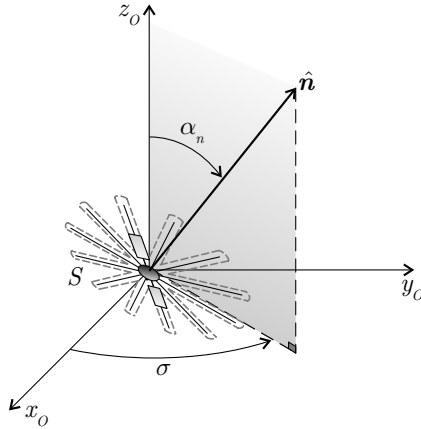
4

Figure 4: Sail pitch and clock angles.

From Eqs. (1) and (2), the components of the propulsive acceleration vector in $\mathcal{T}_O$ are

$$[\boldsymbol{a}]_{\mathcal{T}_O} = \begin{bmatrix} a_{x_O} \\ a_{y_O} \\ a_{z_O} \end{bmatrix} \triangleq \frac{\kappa \, a_c}{2} \left(\frac{r_\oplus}{r} \right) \begin{bmatrix} \cos\alpha_n \, \sin\alpha_n \, \cos\sigma \\ \cos\alpha_n \, \sin\alpha_n \, \sin\sigma \\ \cos^2\alpha_n + 1 \end{bmatrix} \tag{3}$$

whose magnitude a depends on the thrust modulation parameter κ and the sail pitch angle α_n as

$$a = \frac{\kappa \, a_c}{2} \left(\frac{r_\oplus}{r} \right) \sqrt{4 - 3 \sin^2\alpha_n} \tag{4}$$

Figure 5 shows the ratio a/a_c as a function of the pitch angle α_n when $r = r_\oplus$ and $\kappa = \{0.2, 0.4, 0.6, 0.8, 1\}$. In the special case when $\kappa = 1$ and $r = r_\oplus$, Eq. (4) states that $a = a_c$ if $\alpha_n = 0$ (that is, $\hat{\boldsymbol{n}} \equiv \hat{\boldsymbol{r}}$), which is referred to as Sun-facing sail [27, 28]; see Fig. 4.
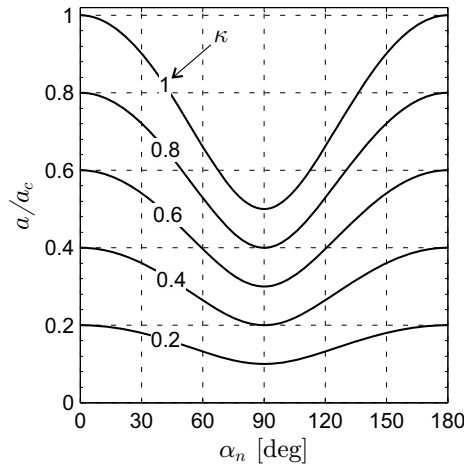

Figure 5: Dimensionless magnitude of propulsive acceleration when $r = r_\oplus$; see Eq. (4).

2.1. Equations of motion

The heliocentric motion of the E-sail-based spacecraft is now analyzed in a cylindrical reference frame $\mathcal{T}_C(O; \rho, \theta, z)$, where ρ (or z) is the scalar projection of the Sun-spacecraft position vector $\boldsymbol{r}$ on the ecliptic plane (or along the z_I-axis), and θ is the polar angle measured counterclockwise from the vernal equinox direction; see Fig. 6. The Sun-spacecraft distance is

$$r = \sqrt{\rho^2 + z^2} \tag{5}$$

5

whereas the spacecraft azimuth angle $\phi \in [0, \pi]$ rad, that is, the angle between the z_I-axis and the Sun-spacecraft line O-S, is given by

$$\sin \phi = \frac{\rho}{\sqrt{\rho^2 + z^2}} \qquad , \qquad \cos \phi = \frac{z}{\sqrt{\rho^2 + z^2}} \tag{6}$$
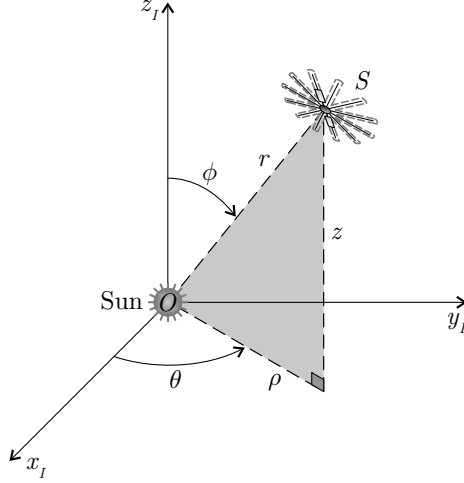

Figure 6: Cylindrical reference frame $\mathcal{T}_C$.

The spacecraft equations of motion in the cylindrical reference frame $\mathcal{T}_C$ are

$$\ddot{\rho} - \rho \dot{\theta}^2 = a_\rho - \frac{\mu_\odot \, \rho}{r^3} \tag{7}$$

$$\rho \ddot{\theta} + 2 \dot{\rho} \dot{\theta} = a_\theta \tag{8}$$

$$\ddot{z} = a_z - \frac{\mu_\odot \, z}{r^3} \tag{9}$$

where $\mu_\odot$ is the Sun's gravitational parameter, and $\{a_\rho, a_\theta, a_z\}$ are the components of the E-sail propulsive acceleration vector in $\mathcal{T}_C$, or $[\boldsymbol{a}]_{\mathcal{T}_C} = [a_\rho, a_\theta, a_z]^{\mathrm{T}}$. Note that Eqs. (7)–(9) model the spacecraft heliocentric dynamics when all orbital perturbations are neglected. The latter assumption is reasonable in a preliminary trajectory design phase. Using the fact that

$$[\boldsymbol{a}]_{\mathcal{T}_C} = \begin{bmatrix} \cos \phi & 0 & \sin \phi \\ 0 & 1 & 0 \\ -\sin \phi & 0 & \cos \phi \end{bmatrix} [\boldsymbol{a}]_{\mathcal{T}_O} \equiv \begin{bmatrix} a_{x_O} \, \cos \phi + a_{z_O} \, \sin \phi \\ a_{y_O} \\ a_{z_O} \, \cos \phi - a_{x_O} \, \sin \phi \end{bmatrix} \tag{10}$$

the components of $[\boldsymbol{a}]_{\mathcal{T}_C}$ can be rewritten as a function of the coordinates $\{\rho, z\}$ and the control variables $\{\kappa, \alpha_n, \sigma\}$ by substituting Eqs. (3) and (5)-(6) in Eq. (10). The result is

$$[\boldsymbol{a}]_{\mathcal{T}_C} = \begin{bmatrix} a_\rho \\ a_\theta \\ a_z \end{bmatrix} = \frac{\kappa \, a_c \, r_\oplus}{2 \, (\rho^2 + z^2)} \begin{bmatrix} \rho \cos^2 \alpha_n + z \sin \alpha_n \, \cos \alpha_n \, \cos \sigma + \rho \\ \cos \alpha_n \, \sin \alpha_n \, \sin \sigma \, \sqrt{\rho^2 + z^2} \\ z \cos^2 \alpha_n - \rho \sin \alpha_n \, \cos \alpha_n \, \cos \sigma + z \end{bmatrix} \tag{11}$$

Substituting Eq. (11) into (7)–(9), the spacecraft dynamics is expressed as a set of first order differential

equations as

$$\dot{\rho} = v_\rho \tag{12}$$

$$\dot{\theta} = \frac{v_\theta}{\rho} \tag{13}$$

$$\dot{z} = v_z \tag{14}$$

$$\dot{v}_\rho = \frac{v_\theta^2}{\rho} - \frac{\mu_\odot \, \rho}{(\rho^2 + z^2)^{3/2}} + \frac{\kappa \, a_c \, r_\oplus}{2 \, (\rho^2 + z^2)} \left(\rho \cos^2 \alpha_n + z \, \sin \alpha_n \, \cos \alpha_n \, \cos \sigma + \rho \right) \tag{15}$$

$$\dot{v}_\theta = -\frac{v_\rho \, v_\theta}{\rho} + \frac{\kappa \, a_c \, r_\oplus}{2 \, (\rho^2 + z^2)} \cos \alpha_n \, \sin \alpha_n \, \sin \sigma \, \sqrt{\rho^2 + z^2} \tag{16}$$

$$\dot{v}_z = -\frac{\mu_\odot \, z}{(\rho^2 + z^2)^{3/2}} + \frac{\kappa \, a_c \, r_\oplus}{2 \, (\rho^2 + z^2)} \left(z \cos^2 \alpha_n - \rho \, \sin \alpha_n \, \cos \alpha_n \, \cos \sigma + z \right) \tag{17}$$

where $\{v_\rho, \, v_\theta, \, v_z\}$ are the components of the spacecraft (inertial) velocity vector in $\mathcal{T}_C$. Equations (12)–(17) may be more conveniently written in a dimensionless form by using $r_\oplus$ as the distance unit, and introducing the dimensionless time

$$\tau \triangleq \frac{t}{t_f} \qquad \text{with} \qquad \tau \in [0, \, 1] \tag{18}$$

where $t \in [0, \, t_f]$ is the time, and t_f is the total flight time. The result is

$$\widetilde{\rho}' = \widetilde{v}_{\widetilde{\rho}} \triangleq f_{\widetilde{\rho}} \tag{19}$$

$$\theta' = \frac{\widetilde{v}_\theta}{\widetilde{\rho}} \triangleq f_\theta \tag{20}$$

$$\widetilde{z}' = \widetilde{v}_{\widetilde{z}} \triangleq f_{\widetilde{z}} \tag{21}$$

$$\widetilde{v}'_{\widetilde{\rho}} = \frac{\widetilde{v}_\theta^2}{\widetilde{\rho}} - \frac{\widetilde{\mu}_\odot \, \widetilde{\rho}}{(\widetilde{\rho}^2 + \widetilde{z}^2)^{3/2}} + \frac{\kappa \, \widetilde{a}_c}{2} \left(\widetilde{\rho} \cos^2 \alpha_n + \widetilde{z} \, \sin \alpha_n \, \cos \alpha_n \, \cos \sigma + \widetilde{\rho} \right) \triangleq f_{\widetilde{v}_{\widetilde{\rho}}} \tag{22}$$

$$\widetilde{v}'_\theta = -\frac{\widetilde{v}_{\widetilde{\rho}} \, \widetilde{v}_\theta}{\widetilde{\rho}} + \frac{\kappa \, \widetilde{a}_c}{2} \cos \alpha_n \, \sin \alpha_n \, \sin \sigma \, \sqrt{\widetilde{\rho}^2 + \widetilde{z}^2} \triangleq f_{\widetilde{v}_\theta} \tag{23}$$

$$\widetilde{v}'_{\widetilde{z}} = -\frac{\widetilde{\mu}_\odot \, \widetilde{z}}{(\widetilde{\rho}^2 + \widetilde{z}^2)^{3/2}} + \frac{\kappa \, \widetilde{a}_c}{2} \left(\widetilde{z} \cos^2 \alpha_n - \widetilde{\rho} \, \sin \alpha_n \, \cos \alpha_n \, \cos \sigma + \widetilde{z} \right) \triangleq f_{\widetilde{v}_{\widetilde{z}}} \tag{24}$$

where the superscript $'$ represents a derivative with respect to τ, and

$$\widetilde{\rho} \triangleq \frac{\rho}{r_\oplus} \quad , \quad \widetilde{z} \triangleq \frac{z}{r_\oplus} \quad , \quad \widetilde{\mu}_\odot \triangleq \frac{\mu_\odot \, t_f^2}{r_\oplus^3} \quad , \quad \widetilde{a}_c \triangleq \frac{a_c \, t_f^2}{r_\oplus} \quad ,$$

$$\widetilde{v}_{\widetilde{\rho}} \triangleq \frac{v_\rho \, t_f}{r_\oplus} \quad , \quad \widetilde{v}_\theta \triangleq \frac{v_\theta \, t_f}{r_\oplus} \quad , \quad \widetilde{v}_{\widetilde{z}} \triangleq \frac{v_z \, t_f}{r_\oplus} \tag{25}$$

The equivalent vector form of the previous system of differential equations is

$$\boldsymbol{x}'(\tau) = \boldsymbol{f}(\boldsymbol{x}, \boldsymbol{u}) \tag{26}$$

where $\boldsymbol{f} \triangleq [f_{\widetilde{\rho}}, f_\theta, f_{\widetilde{z}}, f_{\widetilde{v}_{\widetilde{\rho}}}, f_{\widetilde{v}_\theta}, f_{\widetilde{v}_{\widetilde{z}}}]^{\mathrm{T}}$, whose scalar components are reported in Eqs. (19)–(24), $\boldsymbol{x}$ is the dimensionless state vector defined as

$$\boldsymbol{x} \triangleq [\widetilde{\rho}, \, \theta, \, \widetilde{z}, \, \widetilde{v}_{\widetilde{\rho}}, \, \widetilde{v}_\theta, \, \widetilde{v}_{\widetilde{z}}]^{\mathrm{T}} \tag{27}$$

and $\boldsymbol{u}$ is the control vector, given by

$$\boldsymbol{u} \triangleq [\kappa, \, \alpha_n, \, \sigma]^{\mathrm{T}} \tag{28}$$

The system of differential equations (26) is completed by the initial condition $\boldsymbol{x}(0) = \boldsymbol{x}_0$. Note that the six components of $\boldsymbol{x}_0$ univocally define the parking orbit characteristics and the spacecraft (angular) position along that orbit.

3. Problem description and trajectory optimization

For a fixed value of t_f and a given control law $\boldsymbol{u}(\tau)$, the numerical integration of Eq. (26) with the initial condition $\boldsymbol{x}(0) = \boldsymbol{x}_0$ gives the spacecraft heliocentric trajectory in terms of components of the state vector $\boldsymbol{x}$. In a typical mission scenario of an E-sail-based spacecraft [22, 29] the value of t_f and the control law $\boldsymbol{u} = \boldsymbol{u}(\tau)$ are chosen such as to minimize the flight time required to reach a prescribed final state (subscript f), that is, $\boldsymbol{x}(1) = \boldsymbol{x}_f$ is given. This happens, for example, in an interplanetary rendezvous mission, where $\boldsymbol{x}_0$ coincides with the state of the starting planet and $\boldsymbol{x}_f$ with that of the arrival planet. The problem is therefore to maximize the performance index

$$J \triangleq -t_f \tag{29}$$

with the constraints in the control variables along the whole transfer trajectory

$$\kappa \in [0, 1] \cap \alpha_n \in [0, \pi/2] \,\text{rad} \tag{30}$$

and the boundary constraints

$$\boldsymbol{x}(0) = \boldsymbol{x}_0 \cap \boldsymbol{x}(1) = \boldsymbol{x}_f \tag{31}$$

Note that the constraints on the control variables $\{\kappa, \alpha_n\}$ defined in Eqs. (30) can be related to the components of the propulsive acceleration $\{a_{x_O}, a_{y_O}, a_{z_O}\}$ and interpreted in a graphical way. To that end, assume that $\alpha_n \neq 0$ and introduce the transverse unit vector $\hat{\boldsymbol{t}} \triangleq [(\hat{\boldsymbol{r}} \times \hat{\boldsymbol{n}}) \times \hat{\boldsymbol{r}}]/\sin\alpha_n$. The propulsive acceleration vector lies on the plane spanned by $\hat{\boldsymbol{r}}$ and $\hat{\boldsymbol{t}}$ since it may be written in terms of radial and transverse components as [19]

$$\boldsymbol{a} = a_c \left(\frac{r_\oplus}{r}\right) \left(\tilde{a}_r \, \hat{\boldsymbol{r}} + \tilde{a}_t \, \hat{\boldsymbol{t}}\right) \tag{32}$$

where

$$\tilde{a}_r = \kappa \, \frac{\cos^2\alpha_n + 1}{2} \tag{33}$$

$$\tilde{a}_t = \kappa \, \frac{\sin\alpha_n \, \cos\alpha_n}{2} \tag{34}$$

A comparison between Eq. (33) and Eq. (3) reveals that

$$a_r \triangleq \tilde{a}_r \, a_c \left(\frac{r_\oplus}{r}\right) \equiv a_{z_O} \tag{35}$$

$$a_t \triangleq \tilde{a}_t \, a_c \left(\frac{r_\oplus}{r}\right) = \sqrt{a_{x_O}^2 + a_{y_O}^2} \tag{36}$$

Upon combining Eqs. (33) and (34) it may be verified that

$$\tilde{a}_t^2 + \left(\tilde{a}_r - \frac{3}{4}\kappa\right)^2 = \left(\frac{\kappa}{4}\right)^2 \tag{37}$$

which represents the equation of a circle in the plane $(\tilde{a}_t, \tilde{a}_r)$ with center at $(0, 3\kappa/4)$ and radius equal to $\kappa/4$. Figure 7 shows the dimensionless propulsive acceleration components for different values of κ. Note that, when κ is continuously varied in its range $[0, 1]$, the circles described by Eq. (37) define a region $\mathcal{S}$ within which the dimensionless propulsive acceleration is constrained to lie. Recall also that $\alpha_n \in [0, \pi/2]\,\text{rad}$ because $\hat{\boldsymbol{n}}$ always points in the direction opposite to the Sun. An interesting property is related to the tangent to the circle of Eq. (37) from the origin, which is drawn in Fig. 8 for a given value of κ. With the aid of the geometry in the figure, it may be seen that the equation of that tangent is $\tilde{a}_r = 2\sqrt{2}\,\tilde{a}_t$ and is
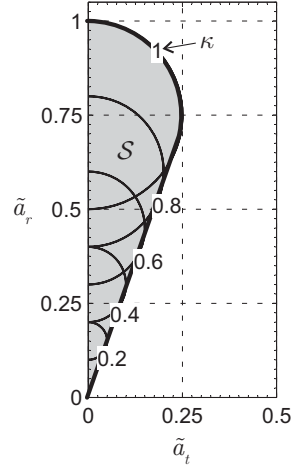
Figure 7: Dimensionless propulsive acceleration components and admissible region $\mathcal{S}$ (shaded area) for the propulsive acceleration.
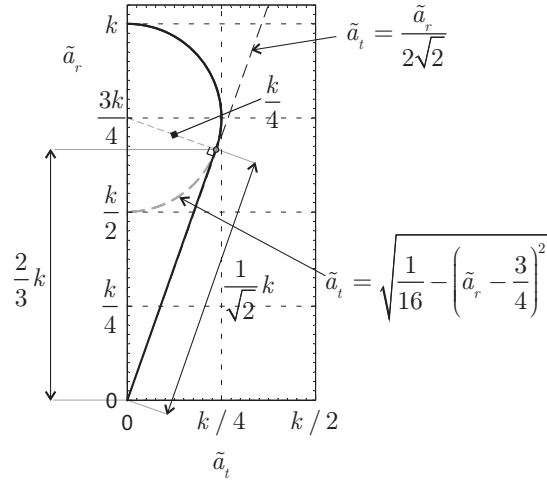

Figure 8: Geometrical analysis of the region $\mathcal{S}$.

therefore independent of κ. This implies that the lower bound of the admissible region $\mathcal{S}$ is actually a line with a slope equal to $2\sqrt{2}$. The whole region $\mathcal{S}$ can therefore be written as

$$
\mathcal{S} = \{\widetilde{a}_t, \widetilde{a}_t\} :
\begin{cases}
\widetilde{a}_t \leq \dfrac{\widetilde{a}_r}{2\sqrt{2}} & \text{if} \quad \widetilde{a}_r \in [0,\, 2/3] \\[4mm]
\widetilde{a}_t \leq \sqrt{\dfrac{1}{16} - \left(\widetilde{a}_r - \dfrac{3}{4}\right)^2} & \text{if} \quad \widetilde{a}_r \in [2/3,\, 1]
\end{cases}
\tag{38}
$$

Finally, Eqs. (35) and (36) may be used to check whether or not the propulsive acceleration components $\{a_{x_O}, a_{y_O}, a_{z_O}\}$ are consistent with the constraints of Eq. (30). In fact, at a given Sun-spacecraft distance r and for an assigned characteristic acceleration a_c, the constraints to be met are

$$
\sqrt{a_{x_O}^2 + a_{y_O}^2} \leq \frac{a_{z_O}}{2\sqrt{2}} \qquad \text{if} \qquad \frac{a_{z_O}}{a_c\,(r_\oplus/r)} \in [0,\, 2/3]
\tag{39}
$$

$$
\sqrt{a_{x_O}^2 + a_{y_O}^2} \leq a_c\,\frac{r_\oplus}{r}\,\sqrt{\frac{1}{16} - \left[\frac{a_{z_O}}{a_c\,(r_\oplus/r)} - \frac{3}{4}\right]^2} \qquad \text{if} \qquad \frac{a_{z_O}}{a_c\,(r_\oplus/r)} \in [2/3,\, 1]
\tag{40}
$$

9

3.1. Approximation using Bezier functions

Using a shape-based approach [7] for the optimal transfer trajectory design, the components of the spacecraft (dimensionless) position vector $\{\widetilde{\rho}, \theta, \widetilde{z}\}$ are now expanded in the domain of τ using Bezier functions [12, 13] of order $n \in \mathbb{N} \geq 3$, given by

$$i(\tau) = \sum_{j=0}^{n} B_j(\tau)\, P_{i,j} \qquad \text{with} \qquad i = \{\widetilde{\rho},\, \theta,\, \widetilde{z}\} \tag{41}$$

where $P_{i,j}$ are the unknown geometric coefficients (i.e., the so called control points), and $B_j(\tau)$ are the Bernstein basis polynomials of degree n, defined as

$$B_j(\tau) = \frac{n!\, \tau^j\, (1-\tau)^{n-j}}{j!\, (n-j)!} \qquad \text{with} \qquad j \in \{1, 2, \ldots, n\} \tag{42}$$

In general, a different value of n can be chosen for each spacecraft state (that is, n_ρ, n_θ, and n_z). However, for the sake of simplicity, this work considers the same value of n for all state variables.

Taking into account Eqs. (41) and (42), the first and the second τ-derivatives of the ith-coordinate approximation can be written, in a compact form, as

$$i'(\tau) \equiv \widetilde{v}_i = \sum_{j=0}^{n} B_j'(\tau)\, P_{i,j} \qquad \text{with} \qquad i = \{\widetilde{\rho},\, \theta,\, \widetilde{z}\} \tag{43}$$

and

$$i''(\tau) \equiv \widetilde{v}_i' = \sum_{j=0}^{n} B_j''(\tau)\, P_{i,j} \qquad \text{with} \qquad i = \{\widetilde{\rho},\, \theta,\, \widetilde{z}\} \tag{44}$$

where

$$B_j'(\tau) = \begin{cases} -n\,(1-\tau)^{n-1} & \text{if} \quad j = 0 \\[2mm] \dfrac{n!\,\tau^{j-1}\,(1-\tau)^{n-j}}{(j-1)!\,(n-j)!} - \dfrac{n!\,\tau^j\,(1-\tau)^{n-j-1}}{j!\,(n-j-1)!} & \text{if} \quad j \in [1,\, n-1] \\[3mm] n\,\tau^{n-1} & \text{if} \quad j = n \end{cases} \tag{45}$$

and

$$B_j''(\tau) = \begin{cases} n\,(n-1)\,(1-\tau)^{n-2} & \text{if} \quad j = 0 \\[2mm] n\,(n-1)\,(n-2)\,\tau(1-\tau)^{n-3} - 2n(n-1)(1-\tau)^{n-2} & \text{if} \quad j = 1 \\[2mm] \dfrac{n!\,\tau^{j-2}\,(1-\tau)^{n-j}}{(j-2)!\,(n-j)!} - \dfrac{2n!\,\tau^{j-1}\,(1-\tau)^{n-j-1}}{(j-1)!(n-j-1)!} + \dfrac{n!\,\tau^j\,(1-\tau)^{n-j-2}}{j!\,(n-j-2)!} & \text{if} \quad j \in [2,\, n-2] \\[3mm] n\,(n-1)\,(n-2)\,\tau^{n-3}\,(1-\tau) - 2\,n\,(n-1)\,\tau^{n-2} & \text{if} \quad j = n-1 \\[2mm] n\,(n-1)\,\tau^{n-2} & \text{if} \quad j = n \end{cases} \tag{46}$$

In particular, the boundary values of B_j and B_j' are obtained by substituting $\tau = 0$ (initial time instant), or $\tau = 1$ (final time instant) into Eqs. (42) and (45), viz.

$$B_j(0) = \begin{cases} 1 & \text{if} \quad j = 0 \\ 0 & \text{if} \quad j \in [1,\, n] \end{cases} \tag{47}$$

$$B_j(1) = \begin{cases} 0 & \text{if} \quad j \in [0,\, n-1] \\ 1 & \text{if} \quad j = n \end{cases} \tag{48}$$

10

$$B'_j(0) = \begin{cases} -n & \text{if} & j = 0 \\ n & \text{if} & j = 1 \\ 0 & \text{if} & j \in [2,\, n] \end{cases} \tag{49}$$

$$B'_j(1) = \begin{cases} 0 & \text{if} & j \in [0,\, n-2] \\ -n & \text{if} & j = n-1 \\ n & \text{if} & j = n \end{cases} \tag{50}$$

Using Eqs. (41) and (43), the boundary value of the generic dimensionless ith-coordinate approximation and its first τ-derivative are given by

$$i(0) = P_{i,0} \ , \ i(1) = P_{i,n} \ , \ \widetilde{v}_i(0) = n\,(P_{i,1} - P_{i,0}) \ , \ \widetilde{v}_i(1) = n\,(P_{i,n} - P_{i,n-1}) \tag{51}$$

with $i = \{\widetilde{\rho}, \theta, \widetilde{z}\}$. The twelve geometric coefficients $\{P_{i,0},\, P_{i,1},\, P_{i,n},\, P_{i,n-1}\}$ can be obtained, as a function of the (given) components of the spacecraft state vector at the initial and the (unknown) final time t_f, by combining Eqs. (25) with Eqs. (19)–(21) and (51). The result is

$$P_{\widetilde{\rho},0} = \frac{\rho_0}{r_\oplus} \ , \ P_{\theta,0} = \theta_0 \ , \ P_{\widetilde{z},0} = \frac{z_0}{r_\oplus} \tag{52}$$

$$P_{\widetilde{\rho},1} = \frac{v_{\rho_0}\,t_f}{n\,r_\oplus} + \frac{\rho_0}{r_\oplus} \ , \ P_{\theta,1} = \frac{v_{\theta_0}\,t_f}{n\,r_\oplus} + \theta_0 \ , \ P_{\widetilde{z},1} = \frac{v_{z_0}\,t_f}{n\,r_\oplus} + \frac{z_0}{r_\oplus} \tag{53}$$

$$P_{\widetilde{\rho},n-1} = \frac{\rho_f}{r_\oplus} - \frac{v_{\rho_f}\,t_f}{n\,r_\oplus} \ , \ P_{\theta,n-1} = \theta_f - \frac{v_{\theta_f}\,t_f}{n\,r_\oplus} \ , \ P_{\widetilde{z},n-1} = \frac{z_f}{r_\oplus} - \frac{v_{z_f}\,t_f}{n\,r_\oplus} \tag{54}$$

$$P_{\widetilde{\rho},n} = \frac{\rho_f}{r_\oplus} \ , \ P_{\theta,n} = \theta_f \ , \ P_{\widetilde{z},n} = \frac{z_f}{r_\oplus} \tag{55}$$

Therefore, for a given value of the order $n \geq 3$ of the Bezier functions, the number N_P of unknown geometric coefficients is

$$N_P = 3\,(n+1) - 12 = 3\,n - 9 \tag{56}$$

whereas, bearing in mind that the flight time t_f is an output of the optimization process, the total number N of (scalar) unknowns required to approximate the spacecraft trajectory through Eqs. (41) and (43) is

$$N = N_P + 1 = 3\,n - 8 \tag{57}$$

For a given value of the total flight time t_f, when $n = 3$ Eq. (57) states that $N = 0$ and, therefore, the shape of the transfer orbit is fully determined by the boundary conditions through Eqs. (52)-(55). This feature is similar to the inverse polynomial approach proposed by Wall and Conway [8], and the radial coordinate form discussed by Xie et al. [9]. However, the methods analyzed in Refs. [8, 9] are used in a coplanar transfer of a spacecraft propelled by an electric thruster (i.e., a continuous thrust ion engine) whose thrust vector direction is unconstrained. The Bezier curve-based method proposed in this work, instead, can be used in a three dimensional mission scenario and is flexible enough to model the constraints on the E-sail thrust vector in terms of both its thrust magnitude and direction [19], as is discussed in the next section.

3.2. Trajectory optimization

For a given mission scenario, the problem is to find the minimum-time transfer trajectory such that the constraints of Eqs. (30), or the constraints of Eqs. (39)-(40) are all met. To that end, the components of the propulsive acceleration vector $\{a_{x_O},\, a_{y_O},\, a_{z_O}\}$ are written as a function of the Bezier curve-based approximation given by Eqs. (41) and (43) using the following procedure.

For a given flight time t_f and a set of N_P unknown geometric coefficients $\{P_{i,2}, \ldots, P_{i,n-2}\}$, with $n > 3$ and $i = \{\widetilde{\rho}, \theta, \widetilde{z}\}$, the dimensionless components of the propulsive acceleration can be obtained from

11

Eqs. (22)–(24) by moving the gravitational and inertial terms from the right to the left hand side and using Eqs. (41) and (43) to approximate $\{\widetilde{a}_{\widetilde{\rho}}, \widetilde{a}_{\theta}, \widetilde{a}_{\widetilde{z}}\}$.

The components of the propulsive acceleration $\{a_{\rho}, a_{\theta}, a_z\}$ are then calculated from Eqs. (11), whereas the components $\{a_{x_O}, a_{y_O}, a_{z_O}\}$ may be written, according to Eqs. (6), (10) and (25), as

$$
\begin{bmatrix} a_{x_O} \\ a_{y_O} \\ a_{z_O} \end{bmatrix} = \begin{bmatrix} \cos\phi & 0 & -\sin\phi \\ 0 & 1 & 0 \\ \sin\phi & 0 & \cos\phi \end{bmatrix} \begin{bmatrix} a_{\rho} \\ a_{\theta} \\ a_z \end{bmatrix} \equiv \begin{bmatrix} \dfrac{a_{\rho}\,\widetilde{z} - a_z\,\widetilde{\rho}}{\sqrt{\widetilde{\rho}^2 + \widetilde{z}^2}} \\ a_{\theta} \\ \dfrac{a_{\rho}\,\widetilde{\rho} + a_z\,\widetilde{z}}{\sqrt{\widetilde{\rho}^2 + \widetilde{z}^2}} \end{bmatrix} \tag{58}
$$

Therefore, the transfer trajectory is feasible if the obtained value $\{a_{x_O}, a_{y_O}, a_{z_O}\}$ meets the constraints of Eqs. (39)-(40), see also Fig. 7.

Finally, the values of t_f and $\{P_{i,2}, \ldots, P_{i,n-2}\}$ are obtained by maximizing the performance index J defined in Eq. (29). In other terms, the (continuous) trajectory optimization problem is converted into a smart-scale Nonlinear Programming Problem (NLP) that can be solved using standard numerical methods such as, for example, the interior-point method implemented in the MATLAB built-in function `fmincon` [30]. The convergence criteria used in the simulations are a maximum constraint violation of 1×10^{-9} (TolCon) and a reduction in the cost function of less than 1×10^{-6} (TolFun) in one iteration.

The basic idea to initialize the unknown coefficients in the NLP solver is to provide an approximation of the spacecraft coordinates $\{\rho, \theta, z\}$ at the m Legendre-Gauss discretization points. The unknown coefficients can then be calculated by fitting the functions of Bezier curves through this set of discrete points. Note that the total flight time t_f is a variable that must be optimized. However, the flight time $t_{f_{\text{app}}}$ may be approximated as the ratio of the norm of the vectorial difference between the angular momentum of target and parking orbits to the E-sail torque induced by thrust, viz.

$$
t_{f_{\text{app}}} = \frac{\sqrt{\mu_{\odot}(a_0 + a_f) - 2\,\mu_{\odot}\,\sqrt{a_0\,a_f}\,\cos\Delta i}}{\kappa_{\text{app}}\,a_c\,r_{\oplus}\,\cos\alpha_{n_1}\,\sin\alpha_{n_1}} \tag{59}
$$

where a_0 (or a_f) is the semimajor axis of the parking (or the target) orbit, Δi is the variation in orbital inclination, $\kappa_{\text{app}} \triangleq 1/3$ is the estimated average thrust coefficient, and $\alpha_{n_1} \triangleq 54.7\,\text{deg}$ is the sail pitch angle that maximizes the thrust cone angle [19]. Assuming a third-order Bezier curve ($n = 3$), the approximations of ρ_{app}, θ_{app} and z_{app} can be written as

$$
\rho_{\text{app}}(\tau) = (1 - \tau)^3 P_{\rho,0} + 3\tau(1 - \tau)^2 P_{\rho,1} + 3\tau^2(1 - \tau)P_{\rho,2} + \tau^3 P_{\rho,3} \tag{60}
$$

$$
\theta_{\text{app}}(\tau) = (1 - \tau)^3 P_{\theta,0} + 3\tau(1 - \tau)^2 P_{\theta,1} + 3\tau^2(1 - \tau)P_{\theta,2} + \tau^3 P_{\theta,3} \tag{61}
$$

$$
z_{\text{app}}(\tau) = (1 - \tau)^3 P_{z,0} + 3\tau(1 - \tau)^2 P_{z,1} + 3\tau^2(1 - \tau)P_{z,2} + \tau^3 P_{z,3} \tag{62}
$$

Taking into account the boundary conditions, the control points $P_{i,j}$ are given by

$$
P_{\rho,0} = \rho_i \;,\;\; P_{\rho,1} = \rho_i + t_{f_{\text{app}}}\,\dot{\rho}_i/3 \;,\;\; P_{\rho,2} = \rho_f - t_{f_{\text{app}}}\,\dot{\rho}_f/3 \;,\;\; P_{\rho,3} = \rho_f \tag{63}
$$

$$
P_{\theta,0} = \theta_i \;,\;\; P_{\theta,1} = \theta_i + t_{f_{\text{app}}}\,\dot{\theta}_i/3 \;,\;\; P_{\theta,2} = \theta_f - t_{f_{\text{app}}}\,\dot{\theta}_f/3 \;,\;\; P_{\theta,3} = \theta_f \tag{64}
$$

$$
P_{z,0} = z_i \;,\;\; P_{z,1} = z_i + t_{f_{\text{app}}}\,\dot{z}_i/3 \;,\;\; P_{z,2} = z_f - t_{f_{\text{app}}}\,\dot{z}_f/3 \;,\;\; P_{z,3} = z_f \tag{65}
$$

Consequently, the discrete approximation data values $[\rho_{\text{app}}]_{m\times1}$, $[\theta_{\text{app}}]_{m\times1}$, and $[z_{\text{app}}]_{m\times1}$ can be obtained by substituting $[\tau]_{m\times1}$ into Eqs. (60)–(62). Accordingly, an initial guess for the respected unknown

parameters in Bezier functions can be obtained by using the inverse matrix multiplication procedure.

$$\left[P_{\rho_{\mathrm{app}}}\right]_{(2n-3)\times 1} = \left(\left[B_{\rho_{\mathrm{app}}}\right]_{m\times(2n-3)}\right)^{-1}\left(\left[\rho_{\mathrm{app}}\right]_{m\times 1} - \left[B_{\rho_{\mathrm{app}}}\right]_{m\times 1}\right) \tag{66}$$

$$\left[P_{\theta_{\mathrm{app}}}\right]_{(2n-3)\times 1} = \left(\left[B_{\theta_{\mathrm{app}}}\right]_{m\times(2n-3)}\right)^{-1}\left(\left[\theta_{\mathrm{app}}\right]_{m\times 1} - \left[B_{\theta_{\mathrm{app}}}\right]_{m\times 1}\right) \tag{67}$$

$$\left[P_{z_{\mathrm{app}}}\right]_{(2n-3)\times 1} = \left(\left[B_{z_{\mathrm{app}}}\right]_{m\times(2n-3)}\right)^{-1}\left(\left[z_{\mathrm{app}}\right]_{m\times 1} - \left[B_{z_{\mathrm{app}}}\right]_{m\times 1}\right) \tag{68}$$

4. Numerical Results

The effectiveness of the proposed method is tested in two different ephemeris-constrained missions, the first one simulates an Earth-Mars three-dimensional rendezvous and the second one is a rendezvous with 3671 Dionysus asteroid . The obtained results are then validated by using them as the initial guess in a GPM-based trajectory optimization software [31]. All of the simulations in this paper have been carried out on a personal computer with an Intel processor Core i5-5200U CPU at 2.20 GHz and with 8.00 GB of RAM. In particular, the GPM-based trajectory optimization procedure uses 60 Legendre-Gauss points.

4.1. Earth-Mars transfer

Assume $n = 12$, $a_c = 0.5\,\mathrm{mm/s^2}$, and a launch date on 1st February 2029, that is, a date consistent with the mission scenario discussed in Ref. [29]. In this case, the flight time obtained with the Bezier curve-based method is $t_f \simeq 912\,\mathrm{days}$, whereas the GPM gives a value of about $897\,\mathrm{days}$, that is, a difference of less than 2%. The transfer trajectory obtained with the Bezier curve-based method, and the further optimized trajectory with GPM are illustrated in Fig. 9, in which the scale of the z_I-axis is intentionally exaggerated to better visualize the three-dimensionality of the trajectory.
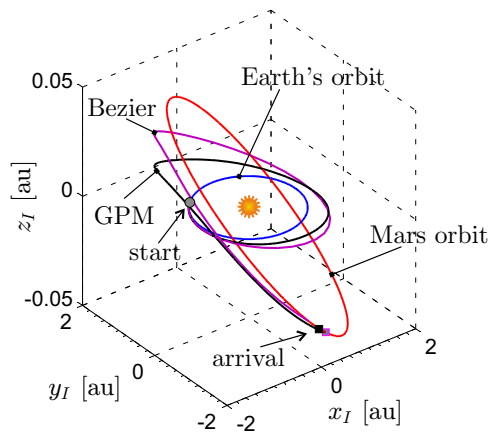

Figure 9: Earth-Mars optimal transfer trajectory with $a_c = 0.5\,\mathrm{mm/s^2}$ and a launch date on 1st February 2029.

Figures 10 and 11 show the time variation of the three components of the spacecraft position and velocity vectors in the inertial reference frame $\mathcal{T}_I$. Note that both the position and the velocity vectors generated by the Bezier and by the GPM method meet the boundary conditions of Eq. (31). This means that the spacecraft successfully entered the sphere of influence of Mars with a small velocity relative to it.

The time histories of the thrust coefficient κ, pitch angle α_n and clock angle σ are illustrated in Fig. 12, where it is worth noting that the Bezier curve-based method gives a good estimate of the optimal time variation of the control variables κ and α_n. In fact, the time curves of control angles generated with the proposed approach are continuous and smooth, which is a very beneficial feature for the attitude tracking control of an E-sail-based spacecraft.
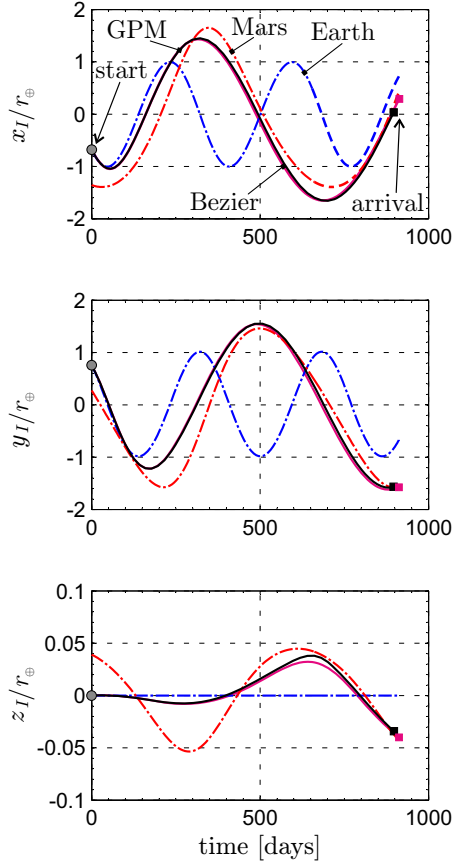
Figure 10: Earth-Mars optimal transfer ($a_c = 0.5$ mm/s^2): time variation of the position vector components in $\mathcal{T}_I$.

a_c [mm/s^2]	t_f [days]		comp. time [s]	
	Bezier	GPM	Bezier	GPM
0.5	912	897	3.7	707
0.6	707	695	4.6	382
0.7	699	683	4.5	679
0.8	676	662	5.1	806
0.9	659	647	7.4	709
1	649	637	9.1	862
1.1	645	632	12.1	882

Table 1: Performance index and computation time for an Earth-Mars transfer with a launch date of 1 February 2029 ($n = 12$).

When the E-sail characteristic acceleration is varied in the range $a_c \in [0.5, 1.1]$mm/s^2, the optimal flight times are summarized in Fig. 13, while Tab. 1 also shows the computational time. In this case, the average difference between the minimum flight times obtained by the Bezier and GPM methods is 1.95% only. In addition, the average computational time with a Bezier approach is about 6.5 s, which corresponds to about 1% of the average computational time used to generate the further optimized trajectory with the GPM. The proposed approach is therefore able to generate an accurate three-dimensional approximation of the optimal transfer trajectory with a reduced simulation time. This is of great significance in the preliminary mission design phase, where a great number of flight scenarios must be analyzed and compared.

4.2. Rendezvous with 3671 Dionysus asteroid

To test the performance of the Bezier-based method in dealing with complex three-dimensional scenarios, a preliminary mission design for the E-sail exploration of 3671 Dionysus asteroid has been analyzed [32].
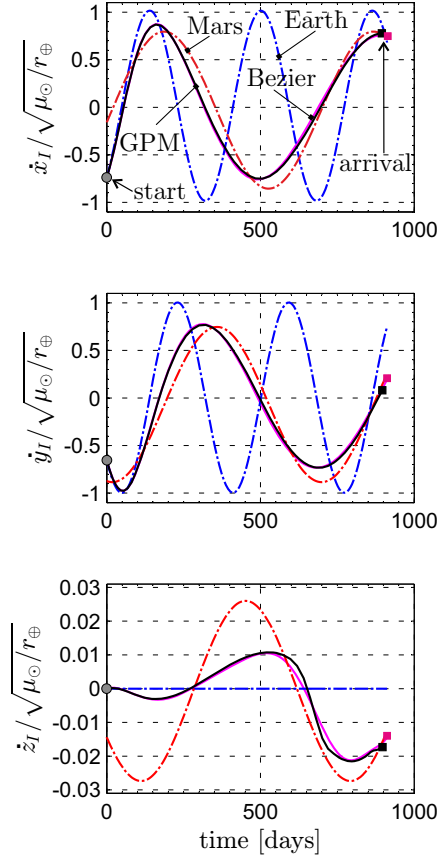
14

Figure 11: Earth-Mars optimal transfer ($a_c = 0.5$ mm/s^2): time variation of the velocity vector components in $\mathcal{T}_I$.

This is certainly a challenging problem from the point of view of the optimal trajectory design, due to the substantial variations in the orbital parameters required to reach the target orbit, characterized by an eccentricity of 0.541 and an inclination of about 13.5 deg.

The trajectory design has been performed. Assuming an optimal Earth-Dionysus transfer with an E-sail characteristic acceleration $a_c = 1$ mm/s^2 and a launch date on March 20, 2024 (the latter is an output of the optimization process), the trajectory generated by the proposed procedure with $n = 20$ Bezier terms and the refined trajectory obtained by the GPM are reported in Fig. 14. The time history of κ and α_n are illustrated in Fig. 15, which shows how the inequality constraints of the E-sail thrust are actually satisfied.

In this case, the total transfer time obtained with the proposed procedure is about 1085 days, while that obtained with the GPM is about 1073 days, with a difference between the solutions of 1.13%. The computational time necessary to generate the initial trajectory with the Bezier functions is 71 s, corresponding to only 0.80% of the computational time reqtired by the GPM. Notably, the computational times used for optimizing the Earth-Dionysus trajectory by the Bezier-based and GPM methods are both longer than those necessary for the Earth-Mars transfer problem. The main reason for this phenomenon is that the challenging Earth-Dionysus transfer problem requires more computational iterations to meet the thrust constraints.

A sensitivity analysis to the order n of the Bezier functions has been conducted assuming again $a_c = 1$ mm/s^2, and the results are summarized in Tab. 2. Note that, in this involved problem, the proposed procedure gives a optimal flight time substantially independent of the order of the Bezier functions when $n \geq 20$, whereas the computational time rapidly grows with n.
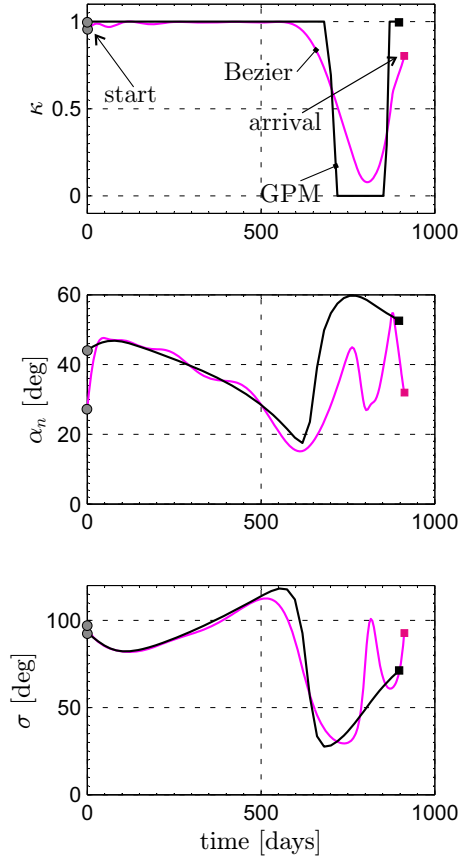
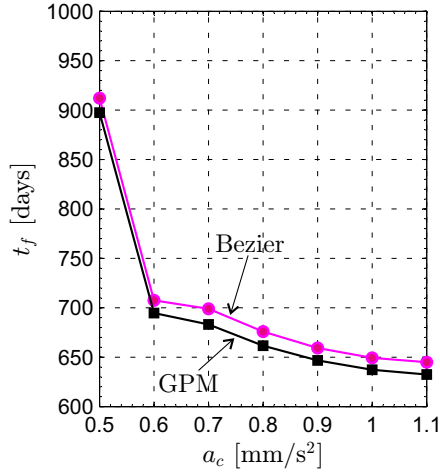Figure 12: Earth-Mars optimal transfer ($a_c = 0.5$ mm/s^2): time variation of the control variables.

Figure 13: Minimum flight times as a function of a_c for an Earth-Mars transfer with a launch date on 1$^{\text{st}}$ February 2029.

Conclusions

In this paper, the preliminary design of an optimal transfer trajectory of an Electric Solar Wind Sail spacecraft is obtained through a Bezier curve-based shape method. In this context, the (dimensionless) time variation of the spacecraft position vector components is assumed to have the form of Bezier curve function and, for a typical interplanetary rendezvous mission scenario, the boundary constraints are satisfied by enforcing the value of twelve geometric coefficients. In particular, the proposed method allows the thrust
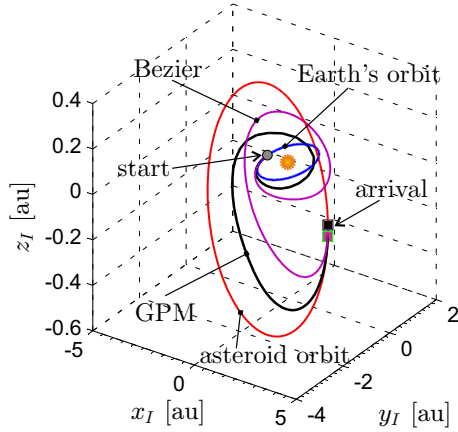
Figure 14: Optimal transfer trajectory towards 3671 Dionysus asteroid with $a_c = 1$ mm/s^2 and a launch date on 20$^{\text{th}}$ March 2024.
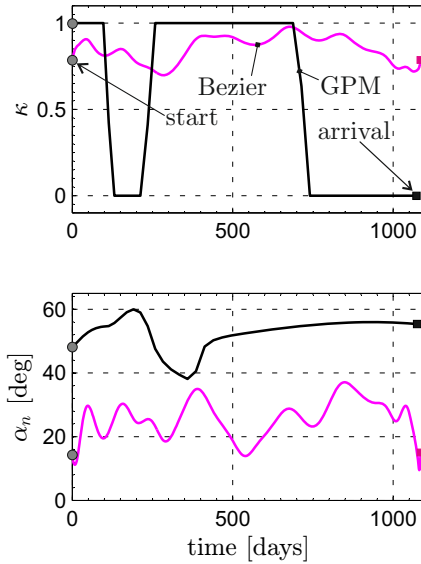

Figure 15: Transfer trajectory towards 3671 Dionysus asteroid with $a_c = 1$ mm/s^2: time variation of κ and α_n.

n	t_f [days]	comp. times [s]
10	1203	32
15	1100	58
20	1085	71
30	1081	182
40	1078	320

Table 2: Performance index and computation time for a transfer towards 3671 Dionysus asteroid with $a_c = 1$ mm/s^2.

vector constraints to be enforced in a straightforward manner, by using the latest geometrical model of the propulsive acceleration.

The numerical results show that the proposed Bezier curve-based shaping method is able to approximate, with a reduced computational effort, the optimal (that is, the minimum time) three-dimensional transfer trajectory in an Earth-Mars mission scenario, and in a rendezvous with the near-Earth asteroid 3671 Dionysus. This is of great significance for the rapid feasibility assessment of a number of optimal transfer trajectories at the stage of preliminary mission design.

Acknowledgements

References

[1] J. Shan, Y. Ren, Low-thrust trajectory design with constrained particle swarm optimization, Aerospace Science and Technology 36 (2014) 114–124, doi: 10.1016/j.ast.2014.04.004.

[2] H. Ma, S. Xu, Optimization of bounded low-thrust rendezvous with terminal constraints by interval analysis, Aerospace Science and Technology 79 (2018) 58–69, doi: 10.1016/j.ast.2018.05.031.

[3] A. Peloni, A. V. Rao, M. Ceriotti, Automated trajectory optimizer for solar sailing (ATOSS), Aerospace Science and Technology 72 (2018) 465–475, doi: 10.1016/j.ast.2017.11.025.

[4] B. A. Conway, A survey of method available for the numerical optimization of continuous dynamic systems, Journal of Optimization Theory and Applications 152 (2) (2012) 271–306, doi: 10.1007/s10957-011-9918-z.

[5] K. Zeng, Y. Geng, B. Wu, Shape-based analytic safe trajectory design for spacecraft equipped with low-thrust engines, Aerospace Science and Technology 62 (2017) 87–97, doi: 10.1016/j.ast.2016.12.006.

[6] A. A. Quarta, G. Mengali, Minimum-time space missions with solar electric propulsion, Aerospace Science and Technology 15 (5) (2011) 381–392, doi: 10.1016/j.ast.2010.09.003.

[7] A. E. Petropoulos, J. M. Longuski, Shape-based algorithm for the automated design of low-thrust, gravity assist trajectories, Journal of Spacecraft and Rockets 41 (5) (2004) 787–796, doi: 10.2514/1.13095.

[8] B. Wall, B. Conway, Shape-based approach to low-thrust rendezvous trajectory design, Journal of Guidance, Control, and Dynamics 32 (1) (2009) 95–102, doi: 10.2514/1.36848.

[9] C. Xie, G. Zhang, Y. Zhang, Simple shaping approximation for low-thrust trajectories between coplanar elliptical orbits, Journal of Guidance, Control, and Dynamics 38 (12) (2015) 2448–2455, doi: 10.2514/1.G001209.

[10] E. Taheri, O. Abdelkhalik, Initial three-dimensional low-thrust trajectory design, Advances in Space Research 57 (3) (2016) 889–903, doi: 10.1016/j.asr.2015.11.034.

[11] O. Abdelkhalik, E. Taheri, Approximate on-off low-thrust space trajectories using fourier series, Journal of Spacecraft and Rockets 49 (5) (2012) 962–965, doi: 10.2514/1.A32307.

[12] G. Farin, Curves and Surfaces for Computer-Aided Geometric Design: A Practical Guide, Academic Press, 1997, Ch. 4, pp. 44–46, ISBN: 978-0-12-249052-1.

[13] L. Piegl, W. Tiller, The NURBS Book, 2nd Edition, Monographs in Visual Communication, Springer, 1996, Ch. 1, pp. 9–10, ISBN: 978-3-642-97385-7.

[14] P. Janhunen, Electric sail for spacecraft propulsion, Journal of Propulsion and Power 20 (4) (2004) 763–764, doi: 10.2514/1.8580.

[15] P. Janhunen, A. Sandroos, Simulation study of solar wind push on a charged wire: basis of solar wind electric sail propulsion, Annales Geophysicae 25 (3) (2007) 755–767, doi: 10.5194/angeo-25-755-2007.

[16] P. Janhunen, P. Toivanen, J. Polkko, et al., Electric solar wind sail: Towards test missions, Review of Scientific Instruments 81 (11) (2010) 111301 (1–11), doi: 10.1063/1.3514548.

[17] A. A. Quarta, G. Mengali, Minimum-time trajectories of electric sail with advanced thrust model, Aerospace Science and Technology 55 (2016) 419–430, doi: 10.1016/j.ast.2016.06.020.

[18] M. Huo, G. Mengali, A. A. Quarta, Accurate approximation of in-ecliptic trajectories for E-sail with constant pitch angle, Advances in Space Research 61 (10) (2018) 2617–2627, doi: 10.1016/j.asr.2018.02.034.

[19] M. Huo, G. Mengali, A. A. Quarta, Electric sail thrust model from a geometrical perspective, Journal of Guidance, Control and Dynamics 41 (3) (2018) 735–741, doi: 10.2514/1.G003169.

[20] L. Niccolai, A. A. Quarta, G. Mengali, Two-dimensional heliocentric dynamics approximation of an electric sail with fixed attitude, Aerospace Science and Technology 71 (2017) 441–446, doi: 10.1016/j.ast.2017.09.045.

[21] L. Niccolai, A. Anderlini, G. Mengali, A. A. Quarta, Impact of solar wind fluctuations on electric sail mission design, Aerospace Science and Technology 82-83 (2018) 38–45, doi: 10.1016/j.ast.2018.08.032.

[22] G. Mengali, A. A. Quarta, P. Janhunen, Electric sail performance analysis, Journal of Spacecraft and Rockets 45 (1) (2008) 122–129, doi: 10.2514/1.31769.

[23] P. Janhunen, A. A. Quarta, G. Mengali, Electric solar wind sail mass budget model, Geoscientific Instrumentation, Methods and Data Systems 2 (1) (2013) 85–95 .

[24] P. K. Toivanen, P. Janhunen, Electric sailing under observed solar wind conditions, Astrophysics and Space Sciences Transactions 5 (1) (2009) 61–69, doi: 10.5194/astra-5-61-2009.

[25] P. K. Toivanen, P. Janhunen, Spin plane control and thrust vectoring of electric solar sail by tether potential modulation, Journal of Propulsion and Power 29 (1) (2013) 178–185, doi: 10.2514/1.B34330.

[26] P. K. Toivanen, P. Janhunen, Thrust vectoring of an electric sail with a realistic sail shape, Acta Astronautica 131 (2017) 145–151, doi: 10.1016/j.actaastro.2016.11.027.

[27] G. Mengali, A. A. Quarta, G. Aliasi, A graphical approach to electric sail mission design with radial thrust, Acta Astronautica 82 (2) (2013) 197–208, doi: 10.1016/j.actaastro.2012.03.022.

[28] A. A. Quarta, G. Mengali, Analysis of electric sail heliocentric motion under radial thrust, Journal of Guidance, Control and Dynamics 39 (6) (2016) 1431–1435, doi: 10.2514/1.G001632.

[29] M. Huo, G. Mengali, A. A. Quarta, Optimal planetary rendezvous with an electric sail, Aircraft Engineering and Aerospace Technology 88 (4) (2016) 515–522, doi: 10.1108/AEAT-01-2015-0012.

[30] R. H. Byrd, M. E. Hribar, J. Nocedal, An interior point algorithm for large-scale nonlinear programming, SIAM Journal on Optimization 9 (4) (1999) 877–900, doi: 10.1137/S1052623497325107.

[31] D. Benson, A Gauss pseudospectral transcription for optimal control, Ph.D. thesis, Massachusetts Institute of Technology, available at http://dspace.mit.edu/handle/1721.1/28919 (accessed 5 November 2018) (2005).

[32] G. Mengali, A. A. Quarta, Optimal nodal flyby with near-earth asteroids using electric sail, Acta Astronautica 104 (2) (2014) 450–457, doi: 10.1016/j.actaastro.2014.02.012.